ADVANCED MATERIALS TECHNOLOGIES
www.advmattechnol.de

Evaporation Triboelectric-Nanogenerator: Harvesting Low-Grade Heat Energy from Ambient Environment

Hang Qu, Lingyu Wan, Zhiqun Tian, Guanlin Liu, and Zhong Lin Wang**

Although natural evaporation absorbs substantial thermal energy from the ambient environment, efficiently utilizing this high-entropy energy remains challenging. Here, the first water evaporation-induced triboelectric nanogenerator is proposed. It only uses tap water to harvest low-grade heat energy from the surroundings to convert it into electricity. The natural evaporation of the liquid can generate unintermittent electricity with an open-circuit voltage of 382 V, a peak power of 0.42 mW, and three orders of magnitude enhancement up to 59.7 mJ mL^{-1} after consuming the same amount of tap water compared with the droplet-based electricity generators. After which, the excellent power output lights 2 W LED and drives wearable electronic devices. This device also inhibits carbon steel materials' corrosion in solutions through the evaporation effect of the salt water on the spot. The present study provides novel insights for triboelectric nanogenerators regarding energy sources and promotes the practical application of evaporation-power generation technology.

1. Introduction

Energy has always been the ultimate proposition for humanity, and where to obtain it and how to obtain it has been one of the important topics of concern for scientists. The problems of climate change and environmental pollution caused by the massive use of fossil energy are becoming increasingly severe.[1] Searching for renewable energy resources and novel clean energy technologies has become a hot issue.[2] Water, one of the most abundant substances on earth, is an inexhaustible resource as it is recycled in the atmospheric water cycle endlessly.[3,4] It possesses the ability to evaporate at any temperature and air pressure due to the world's inherent inhomogeneity, driven by the fundamental principle of entropy increase.[5,6] The emerging technologies that convert evaporation-related heat energy into electrical energy could serve as an effective strategy to address energy issues. To extract energy from the evaporation process, significant efforts have been made. At present, evaporation-related energy harvesting devices are mainly two kinds. One uses sunlight to increase the steam production rate in the system. The energy of sunlight, stored in the evaporation enthalpy of water vapor through photothermal conversion, can be released with the assistance of thermoelectric modules and pyroelectric nanogenerators.[7–9] This approach requires complex photothermal materials, thermal management, and power generation systems, as well as sunlight, and the energy conversion rate and technical maturity are inferior to those of photovoltaic technology.[10] The other kind of technology is water-evaporation-induced electricity, based on the coulomb interactions occurring at the solid/liquid interface (streaming potential).[11] The ion motion induced by vapor drives the charge carrier motion in the electrode to generate electricity, and this technology was first created in carbon black nanofilms by Zhou in 2017. The subsequent carbon slurry provides a constructive guidance path for such devices' large-scale preparation and integration.[12] As follows, Bian used Ni–Al layered double hydroxides to prepare flexible devices, which simplified the preparation process of materials,[13] while Sun developed high-output power devices by etching silicon wafers.[14] However, in these prevailing evaporation–generation technologies, the absorbed heat energy in the evaporation process hardly finds its way to utilize.

In 2012, triboelectric nanogenerator (TENG) was created that utilizes Maxwell's displacement current to capture high-entropy mechanical energy.[15] It brings us innovative and powerful technologies for electricity generation. It can efficiently convert irregular mechanical energy into electrical energy based on triboelectrification and electrostatic induction effects. Due to its distinct advantages of simple structure,[16,17] material diversity,[18,19] and high energy conversion efficiency,[20,21] TENG

H. Qu, L. Wan, Z. Tian, G. Liu
Center of Nanoenergy Research
Guangxi Colleges and Universities Key Laboratory of Blue Energy and Systems Integration
carbon peak and neutrality science and technology development institute
School of Physical Science & Technology
Guangxi University
Nanning 530004, China
E-mail: lyw2017@gxu.edu.cn
H. Qu, L. Wan, Z. Tian, G. Liu
State Key Laboratory of Featured Metal Materials and Life-cycle Safety for Composite Structures
Nanning 530004, China
Z. L. Wang
Beijing Institute of Nanoenergy and Nanosystems
Chinese Academy of Sciences
Beijing 101400, P. R. China
E-mail: zhong.wang@mse.gatech.edu
The ORCID identification number(s) for the author(s) of this article can be found under https://doi.org/10.1002/admt.202301409

DOI: 10.1002/admt.202301409

has been extensively studied in energy harvesting from ambient environments. To date, TENG has demonstrated its outstanding capabilities in harnessing wind energy,[22,23] kinetic energy of human motion,[24,25] and water wave energy,[26,27] as well as in the development of self-powered sensors and electronic devices.[28,29] Significant progress in the TENG field would greatly promote the use of distributed renewable energy and help alleviate the energy crisis. However, for all we know, current considerable studies mainly focused on those limited environmental scenarios where mechanical energy already exists and left the ubiquitous low-grade heat energy behind.[30,31] If a TENG can capture ambient low-grade heat energy by harnessing the spontaneous energy flow of natural evaporation phenomena, analogous to how an electromagnetic generator utilizes the gravitational potential energy of a liquid flowing from a higher to a lower level, such TENG cannot only broaden the scope of its application but also reshape the previous perceptions of TENG that are only born for mechanical energy.

In this study, therefore, capitalizing on the evaporation–absorption characteristics that yield a spatially heterogeneous heat source, we employ a heat engine as an intermediary and utilize TENG to effectuate the conversion of the captured low-grade heat energy into electrical energy. Based on this, we propose the water evaporation-induced triboelectric nanogenerator (WE-TENG), capable of harvesting heat energy in the everyday environment without relying on any external form of mechanical energy. The evaporation source of the device guides the heat engine (drinking bird) to realize an alternate change of internal pressure, followed by the barycenter, thus generating the movement around the axis. This hard-earned and low-entropy mechanical energy can be efficiently converted into electricity by the elaborately designed non-contact free-rotating disk TENG units in the WE-TENG.[32] It is proven to possess the advantages of robust adaptability, high stability, high output performance, and, more importantly, self-driven operation, which relies on natural evaporation rather than mechanical or fossil energy. With the same amount of tap water consumption, WE-TENG outputs electrical energy three orders of magnitude higher than previous droplet-based electricity generators. Depending on the system's Gibbs free energy change from high to low (spontaneous process), the WE-TENG performs self-operation for an entire day using just a cup of tap water (≈300 mL) without requiring a supply of traditional mechanical energy. The optimized WE-TENG could achieve a peak power of up to 0.42 mW and an open-circuit voltage of 382 V, sufficient to drive two commercial 2 W LED lights and wearable devices. The spontaneous corrosion of carbon steel materials in NaCl solution could be suppressed using the cathodic protection method powered by WE-TENG. Furthermore, the integrated automatic water dispenser aids in accumulating rainwater while improving its maintenance-free and durable functionality. In previous studies on evaporation-generation technology, the important evaporation–absorption characteristics have been largely neglected. However, our research aims to fill this gap by incorporating a heat engine. WE-TENG not only expands the energy source of TENG but also provides valuable conceptual guidance for the advancement of both TENG and evaporation–generation technologies.

2. Results and Discussion

2.1. Working Mechanism of WE-TENG

Heat energy is distributed in considerable amounts in the ambient environment of human existence (Figure S1, Supporting Information), although it remains under-utilized. To harness the widespread ambient thermal energies, a heat engine consisting of a drinking bird is used to absorb heat through the atmospheric evaporation of water and convert these energies into mechanical energy that can be harvested by a TENG, as shown in **Figure 1**a,b. The proposed WE-TENG that harvests low-grade heat energy from the environment by evaporation effect is illustrated in **Figure 2**.

Figure 1b(i) depicts the schematic diagram of the drinking bird structure. The main body of the drinking bird appears similar to that of a bird, with the head and tail formed of glass material with a small spherical shell and a large spherical shell, respectively, which are connected via glass tubes. The front portion of the bird's head protrudes as the beak of the bird. An appropriate amount of diethyl ether is sealed in the cavity of the drinking bird, and in the vertical state, the lower end of the glass tube is immersed in the liquid level. The electrostatic flocking technique is employed to encase nylon fibers around the bird's head surface, with graphene strategically attached to the fibers, effectively enhancing the material's water absorption and evaporation efficiency. The hermetically sealed body is held on a pedestal through a rotor shaft and is able to rotate around this shaft. In the initial state, a small amount of water is used for wetting the composite material, and the water on the composite material absorbs heat because of evaporation. The saturation vapor pressure (P_1) in the small ball decreases with the decrease in temperature (T_1; NOTE S1, Supporting Information). As depicted in Figure 1b(ii), the air pressure in the large ball is greater than that in the small ball, which causes the diethyl ether to rise along the glass tube's inner wall, and the drinking bird's center of gravity shifts up. When the center of gravity of the drinking bird is higher than the rotor shaft, the bird leans forward due to the shift of the center of gravity caused by the beak, as illustrated in Figure 1b(iii). When the drinking bird touches the water cup, the water diffuses into the composite material through capillary force. Meanwhile, the bottom of the glass tube exposes the diethyl ether surface, and the gas in the cavity of the small ball gets connected and mixed with the gas in the large ball. At this point, the diethyl ether in the glass tube flows back to the large sphere under the action of gravity. Finally, the pressure and temperature of the two cavities become consistent, and the drinking bird returns to its initial state, as depicted in Figure 1b(i). Under the coupling effect of rotational inertia and gravitational moment, the drinking bird swings back and forth, as illustrated in Figure 1b(ii), and the diethyl ether rises again along the inner wall of the glass under the action of liquid evaporation. According to these phenomena, the cycle repeats itself. Figure S2, Supporting Information, illustrates the temperature variation curve of the drinking bird during operation.

The subtlety of the drinking bird is that when a cup of water is placed in front of it, it continues "drinking" the water until it is exhausted. If the bird is placed at sea level, the drinking bird

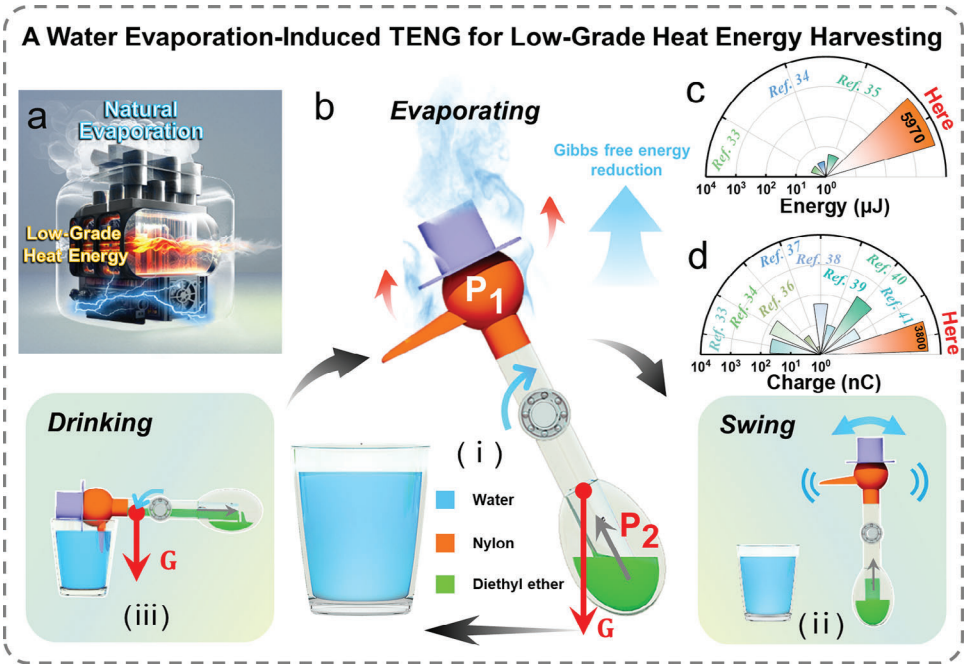

Figure 1. The mechanism and high output performance of the proposed WE-TENG. a) The schematic diagram of WE-TENG. b) The working mechanism of the drinking bird. c) The electrical energy and d) induced charge that the WE-TENG is capable of generating for per 100 μL of tap water consumed.

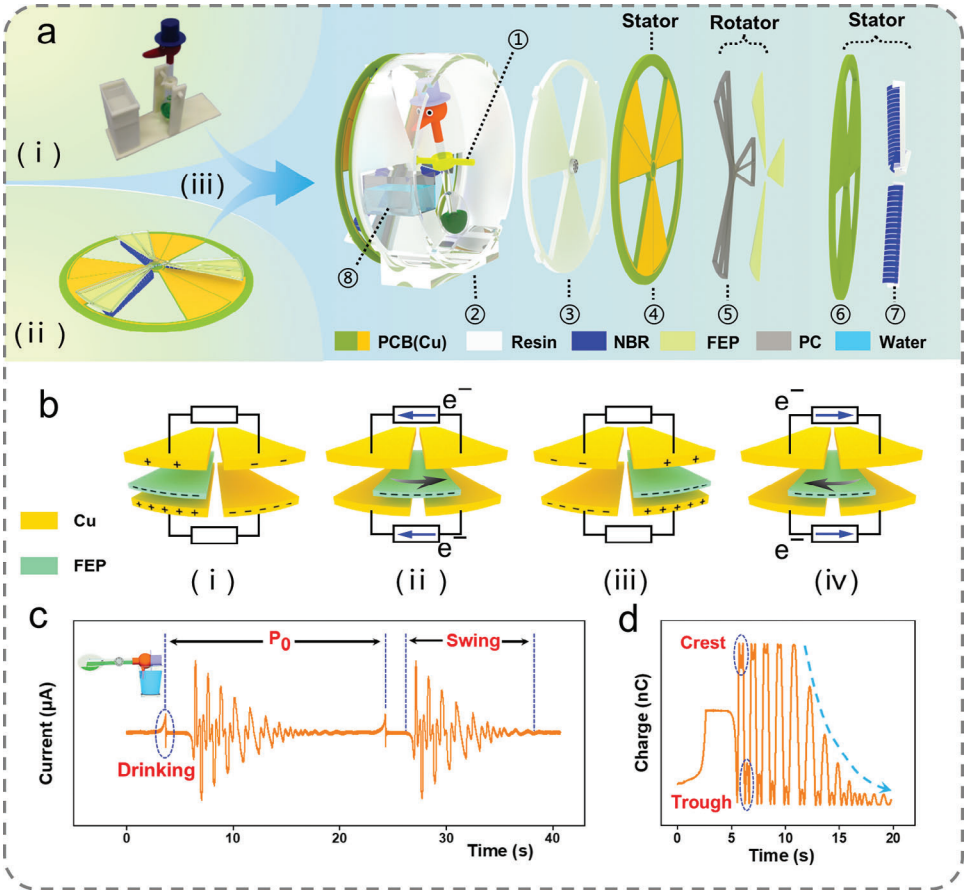

Figure 2. Structure and output characteristics of WE-TENG. a) The architecture diagram of WE-TENG. b) The working mechanism of WE-TENG. c) The short-circuit current waveform, and d) the transferred charge waveform of WE-TENG.

would continuously swing without requiring any artificial input of energy, which would appear as a "perpetual-motion machine". The drinking bird is a heat engine that strictly obeys the laws of thermodynamics (Figure S3, Supporting Information). Its working process includes three phases: absorbing heat, releasing heat, and output of work. The working substance of the drinking bird is diethyl ether vapor in the cavity. The evaporation effect that carries the heat from the diethyl ether vapor is an exothermic process (Q_2). In contrast, transferring heat energy from the environment to the diethyl ether vapor is an endothermic process for the working substance (Q_1). Therefore, the working substance's output work (W) manifests as the flow of diethyl ether and the swing of the drinking bird. The energy utilization efficiency (η) of the drinking bird can be estimated using the formula for heat engine efficiency:

$$\eta = \frac{W}{Q_1} \times 100\% = \frac{E_k}{\nu C_{V,m} \Delta T} \times 100\% \quad (1)$$

where E_k is the kinetic energy of the drinking bird during the swing, ν is the average amount of substance of diethyl ether vapor inside the cavity of the drinking bird during the operation, $C_{V,m}$ is the molar heat capacity at constant volume of the ethyl ether vapor after it has risen halfway, and ΔT is the amount of change in ambient temperature around the drinking bird.

By employing this ingenious heat engine, we have successfully created a WE-TENG for harvesting low-grade heat energy from the natural environment (Figure S4, Supporting Information). The power generation efficiency of the device is presented in Figure 1 (c), where it is demonstrated that the WE-TENG can generate 5.97 mJ (Note S2, Supporting Information) of electrical energy per 100 µL of tap water consumed. This is a remarkable increase in output performance by three orders of magnitude, in comparison to the conventional droplet-based electricity generator (DEG) that uses the gravitational potential energy of water.[33–35] In addition, a comparison was made between the induced charge generated by the WE-TENG and various types of DEGs. Figure 1d demonstrates that the induced charge generated by the WE-TENG is enhanced by an impressive order of magnitude, when compared to the most efficient DEG.[33,34,36–41]

In the present study, WE-TENG was constructed by combining a drinking bird (**Figure 2**a(i)) with a non-contact FRD-TENG (Figure 2a(ii)). As depicted in Figure 2a(iii), the device had three main parts: the dynamical system, the stator, and the water supply device. Since the overall structure of the device is mirror-symmetrical around the vertical plane, one side of the device was used to introduce the structure of the device. As visible in Figure 2a(iii), the dynamic system comprises three parts: the active, transmission, and follower parts. The active part was the drinking bird, which was fixed in the cylinder (②/Figure S5a, Supporting Information) via the rotor shaft (①/Figure S5c, Supporting Information) through the super-lubricated ceramic bearing and the disc (③/Figure S5b, Supporting Information). The drinking bird could swing around the rotor shaft at will. The rotor was the follower part and comprised a fluorinated ethylene propylene copolymer (FEP) film adhered to a polycarbonate (PC) support (⑤/Figure S5d, Supporting Information). The rotor could swing synchronously with the swing of the drinking bird after being connected to the rotor shaft (the transmission part). The stator comprised two pieces of induced electrodes (④ and ⑥/Figure S5e,f, Supporting Information) and three sets of nitrile rubber (NBR) brushes (⑦). With repeated friction, the NBR brush fixed on the outside of the rotor maintained the triboelectric charge for the FEP film during operation. The side with the electrodes prepared on both PCBs faced the rotor forming a sandwich structure, and the distance between the rotor and PCBs was 1.5 mm. Finally, a sink (⑧) was placed in front of the drinking bird and filled with tap water. Further details of the fabrication process are presented in the Experimental Section.

Analogous to the traditional free-standing mode TENG, the FEP swings back and forth, driven by the drinking bird, and rubs against the NBR during the drinking bird's "drinking" process. This process generates positive charges on the NBR and negative charges on the FEP surface (Movie S1, Supporting Information). After several cycles, the charges on the surface of FEP gradually accumulate until saturation is reached. The three groups of fan-shaped electrode units had the same structure. Figure 2b illustrates the process of electrostatic induction at one of these three groups of electrodes. In the initial state, as depicted in Figure 2b(i), the FEP is aligned with the left electrode, and the induced charge opposite the film surface is generated on the electrodes close to the film. Subsequently, the FEP moves to the right under the traction of the drinking bird, as illustrated in Figure 2b(ii). The free electrons on the two pairs of electrodes move from right to left in the external circuit under the action of Coulomb forces until the FEP is aligned with the right electrode, as illustrated in Figure 2b(iii). Figure 2b(iv) illustrates the inverse process of Figure 2b(ii).

With the swings of the drinking bird, WE-TENG generates periodic output signals, and the periodic current waveform of the device is depicted in Figure 2c. The first spike represents the signal when the drinking bird touches the water cup. Even though the FEP film is outside the front region of the electrode, the current is nonetheless generated on the electrode due to the edge effect. The time interval between two adjacent drinking times during the operation of the drinking bird was defined as one operating cycle. Figure 2d depicts the waveform of the transferred charges for one cycle. The depression at the crests and troughs is due to the swing of the rotors beyond the front region of the electrodes, which causes the waveform pattern to drop. After a few signals, a decrease occurred in the wave crest in the second half of the cycle, which is attributable to the gradual tilting of the drinking bird during the rise of the diethyl ether, causing the rotor to appear in an increasingly smaller area in the front region of the electrode.

2.2. Optimization of WE-TENG

In order to improve the output performance of the device, rational structural optimization and material selection are necessary. When using an ordinary metal-rotating shaft, the water that has diffused into the cotton via capillary force would flow to the surface of the large spherical shell along the outer wall of the drinking bird under the action of gravity, which would prolong the operating cycle of the drinking bird. Therefore, an intelligent design with a resin-rotating shaft having grooves and notches was adopted to prevent contact between the water droplets and large

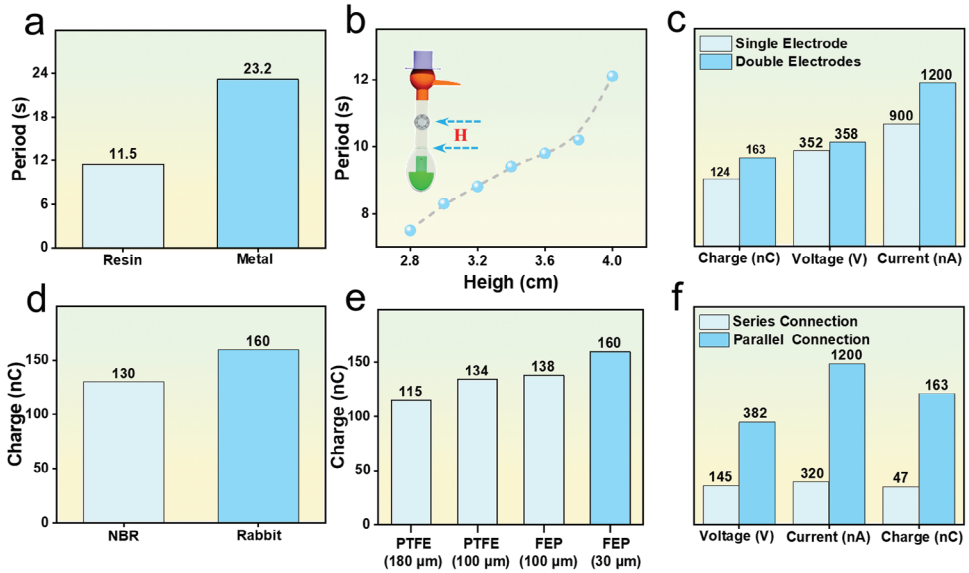

Figure 3. Structural optimization and material selection for the proposed WE-TENG. a) Different types of rotor shafts and b) heights of the rotor shafts on the device during operation. Comparison of the output performance of WE-TENG using c) single and double electrodes, d) rabbit hair brushes and NBR brushes, e) diverse dielectric films, and f) series and parallel connections of four output signals of WE-TENG.

spherical shells via intercepting and draining (Figure S6, Supporting Information). As illustrated in **Figure 3**a, the operating cycle of the drinking bird was 23.2 s long when using the ordinary metal-rotating shaft and was reduced to 11.5 s when using the resin-rotating shaft (ambient temperature: 22 °C, relative humidity: 40%, rotor shaft height: 3.2 mm). This was a 50.4% reduction in the operating cycle. In addition, experimental results revealed a correlation between the drinking bird's operating cycle and rotor shaft height. As presented in Figure 3b, with the increase in the rotor shaft height from 2.8 to 4 cm, the operating cycle of the drinking bird also increased monotonously from 7.5 to 12.1 s (ambient temperature: 27 °C and relative humidity: 31%). This accounts for the fact that the higher the rotor shaft height, the higher the diethyl ether height required to disrupt the equilibrium of the drinking bird, which leads to an increase in the operating cycle of the drinking bird with the increase in the rotor shaft height. Considering that the Coulombic force between the FEP and the electrodes would hamper the "drinking" of the bird, the rotor shaft height was compromised to 3.2 mm in the subsequent experiments to overcome the effect of Coulombic force on the device.

Traditional free-standing TENG in non-contact-sliding mode primarily uses a pair of metal electrodes. In contrast, the proposed WE-TENG uses two pairs of metal electrodes because the output performance of the two pairs of electrodes in parallel is better, as depicted in Figure 3c. The transferred charge of a pair of electrodes is 124 nC, the open-circuit voltage is 352 V, and the short-circuit current is 900 nA. The device with two pairs of electrodes presents a transferred charge of 163 nC, an open-circuit voltage of 382 V (Figure S7, Supporting Information), and a short-circuit current of 1.2 μA. This is because of potential differences on both sides of the FEP film, and the placement of electrodes on both sides could fully exploit this potential difference on both sides of the FEP, thereby improving the output efficiency (Figures S8 and S9, Supporting Information).

The brushes are intermittently in contact with the FEP, effectively replenishing it with charges to maintain a high output performance. Therefore, the ability of FEP to provide electrons to the film is critical. Figure 3d illustrates the output performance of the device when using rabbit hair brushes compared to that when using NBR brushes to replenish the charges of the friction layer (friction layer: FEP with a thickness of 30 μm). Compared to the rabbit brush, the NBR brush increased the transferred charges from 130 nC to 160 nC, the open-circuit voltage from 335 to 382 V (Figure S10, Supporting Information), and the short-circuit current from 0.8 to 1.2 μA. Various friction layers also affected the output performance of the device, as depicted in Figure 3e. FEP (30 μm) exhibited the highest output performance among diverse materials and film thicknesses. The transferred charges reached 160 nC, and the open-circuit voltage reached 382 V (Figure S11, Supporting Information). This could be attributed to two primary reasons: one is that the thinner the dielectric film, the stronger the electrostatic induction effect, and the other reason is that FEP has a more excellent capability of storing electrons on the surface compared to PTFE. Figure 3f presents the output performances after connecting the signals on each of the four PCBs of the device in series and parallel. As visible in the chart, after placing the four groups of signals in parallel, the output performance was better, with an open-circuit voltage of 382 V, a short-circuit current of 1.2 μA, and a transferred charge of 163 nC.

2.3. Output Performance of the Proposed WE-TENG

The different environmental factors, such as temperature, relative humidity (RH), and wind speed, affected the output characteristics of WE-TENG. **Figure 4** presents the output characteristics of the device, including transferred charge, open-circuit voltage, and operating period, at these parameters.

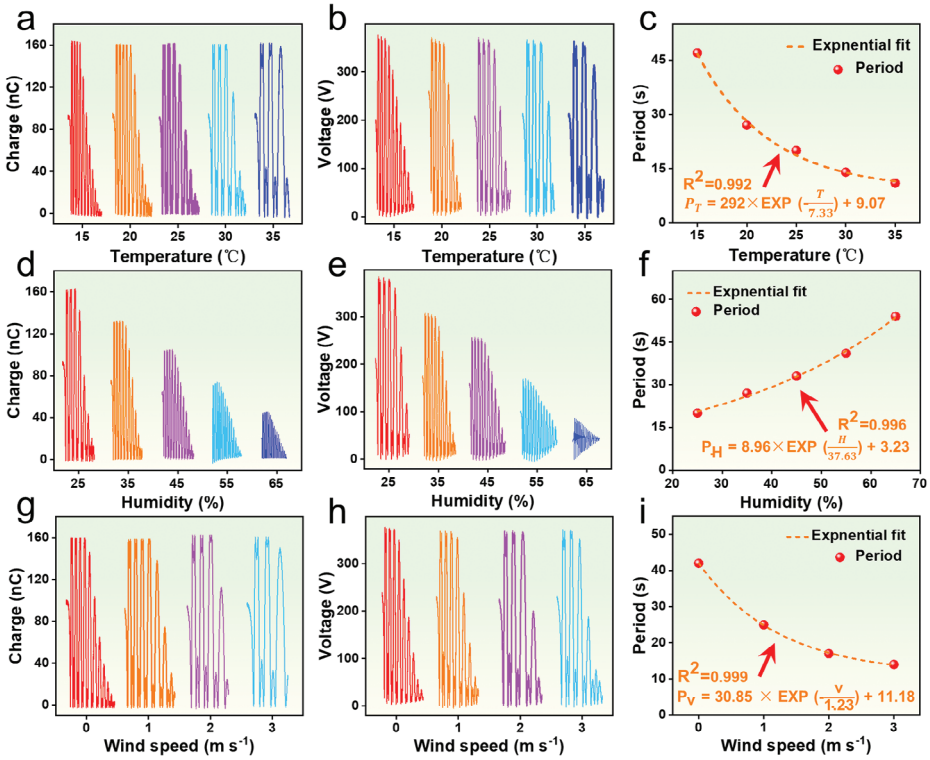

Figure 4. The impact of environmental factors on the proposed device. a) Transferred charge, b) open-circuit voltage, and c) operating period at different temperatures (constants: RH, 25%; wind speed, 0 ms^{-1}). d) The transferred charge, e) open-circuit voltage, and f) operating period at different humidity levels (constants: temperature, 25 °C; wind speed, 0 m s^{-1}). h) The transferred charge, i) open-circuit voltage, and j) operating period at different wind speeds (constants: temperature. 18 °C; RH, 25%).

Figure 4a,b depicts the output waveforms for the device's transferred charge and open-circuit voltage at different ambient temperatures. It could be observed that the transferred charge and open-circuit voltage of the device remained at approximately 160 nC and 380 V, respectively. Previous studies have demonstrated that the output performance of TENG is related to the ambient temperature, which affects the relative dielectric constant of the material, the effective defect, and the hot electron emission.[42,43] In the present study, a slight temperature change was insufficient to significantly alter the triboelectric charges of the FEP, causing the output performance of the device to remain almost the same. Although slight temperature fluctuations cannot significantly influence the triboelectric charge on the film's surface, this may readily affect the liquid's evaporation rate. As depicted in Figure 4c, as the ambient temperature (T) increased gradually from 15 to 35 °C, the operating period (P_T) of the device gradually decreased from 45 to 11 s. This could be attributed to the increased water evaporation rate due to high temperature, which led to a rapid rise of the diethyl ether and, therefore, a shorter operating period for the drinking bird. The following equation may represent the relationship between the two parameters:

$$P_T = 292 \times \mathrm{EXP}\left(-\frac{T}{7.33}\right) + 9.07 \tag{2}$$

The correlation coefficient (R^2) between the data sample and the fitted curve was 0.992, and the operating period demonstrated a high correlation with temperature.

In addition, the effect of RH on the device should not be ignored. As the RH (H) increased from 25% to 65%, the transferred charges (Q_H) decreased from 160 nC to 45 nC (Figure 4d), and the related fitting curve could be expressed as follows:

$$Q_H = -2.91 \times H + 233.06 \tag{3}$$

Further, the open-circuit voltage decreased from 380 to 83 V (Figure 4e), and the operating period of WE-TENG was extended gradually (Figure 4f). The decrease in the output performance could be attributed to the following reason. As RH increased, the water molecules in the air condensed on the surface of the FEP film and formed a water film that released the charges stored on the surface of the dielectric film into the environment.[44] The change in the operating period (P_H) resulted from the coupling of two physical phenomena. The first one was the decelerated water evaporation rate due to the increase in the RH, which resulted in a decelerated rate of rise of diethyl ether. The other one was the decrease in the surface charge density of the FEP film due to the increase in the RH, which reduced the effect of the Coulomb forces on the drinking bird during swinging. The correlation coefficient (R^2) between the data sample and the fitted curve was $R^2 = 0.996$, and the fitted curve could be expressed as follows:

$$P_H = 8.96 \times \mathrm{EXP}\left(\frac{H}{37.63}\right) + 3.23 \tag{4}$$

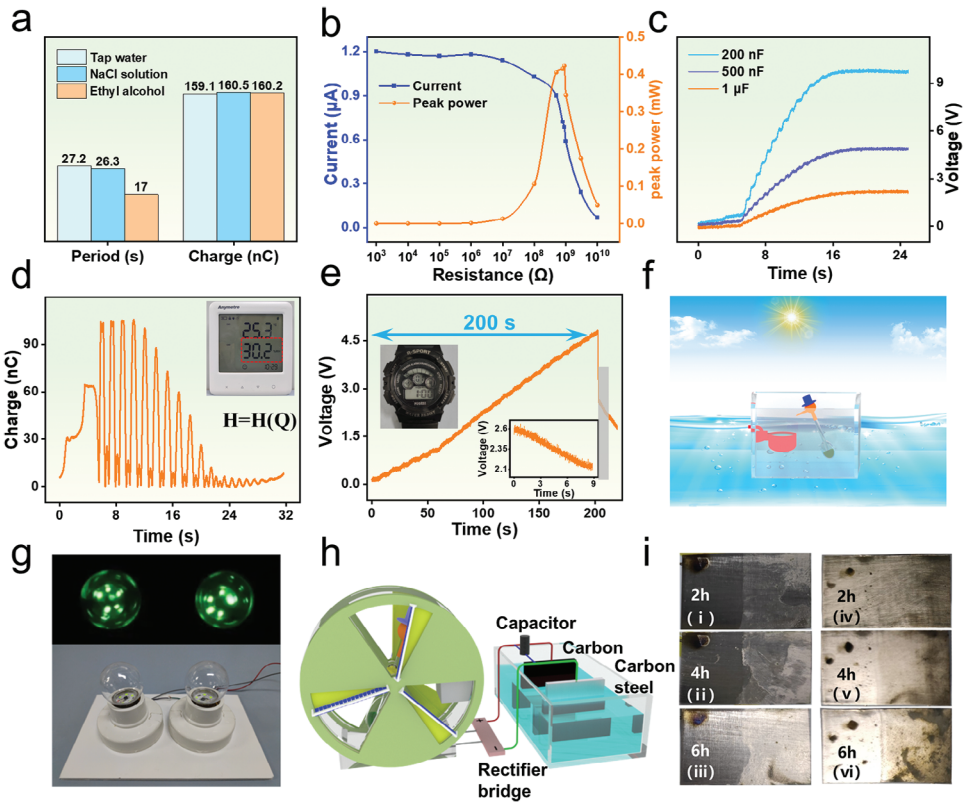

Figure 5. Application. a) Different output performance about different evaporation sources. b) The matching impedance of WE-TENG. c) The charging curves for different commercial capacitors. d) Monitor environmental humidity with WE-TENG. e) Drive electronic watches. f) The application of WE-TENG combined with an automatic water dispenser. g) Light up LEDs (rated power: 2 W). h) The corrosion prevention system constructed using WE-TENG.i) Carbon steel: with cathodic protection, after i) 2 h, ii) 4 h, and iii) 6 h, respectively; and without cathodic protection, after iv) 2 h, v) 4 h, and vi) 6 h, respectively.

Finally, the relationship between the output characteristics of the device and the wind speed was determined. Consistent with the findings of previous studies, different wind speeds did not significantly affect the triboelectric charges on the material surface. The device's transferred charge (Figure 4g, ≈160 nC) and open-circuit voltage (Figure 4h, ≈380 V) remained relatively stable at different wind speeds. However, the flowing air increased the evaporation rate of the liquid, as depicted in Figure 4i, and as the wind speed (v) increased from 0 to 3 m s^{-1}, the operating cycle (P_v) of the device was monotonically reduced from 42 to 14 s. The two parameters were highly correlated according to the following equation:

$$P_v = 30.85 \times \mathrm{EXP}\left(-\frac{v}{1.23}\right) + 11.18, \left(R^2 = 0.999\right) \quad (5)$$

It is noteworthy that an increase in the wind speed from 0 to 1 m s^{-1} could significantly reduce the duration of the operating cycle. This feature was the inspiration to place the WE-TENG in a place with good air circulation during operation to increase the output performance per unit of time.

In our device, the heat absorbed by evaporation acts as a power source to do external work, driving the TENG to produce electrical energy. The factors that affect the performance of the device mainly come from two aspects, one is the evaporation efficiency of the evaporation source and the other is the performance of the TENG. In addition to the inherent properties of the materials, environmental factors such as temperature, humidity, wind speed, etc. have some degree of influence on the device performance. Based on the above experiments, it is noted that the influence of humidity is more pronounced. Higher relative humidity not only affects the evaporation rate of the evaporation source, but also inhibits charge accumulation on the surface of the dielectric material. To further advance the water evaporation-induced triboelectric nanogenerator, materials with higher evaporation efficiency for evaporation source and better resistance to humidity for TENG are highly desired.

2.4. Applications

Besides the environmental parameters, the evaporation source also affected the output characteristics of the proposed device. As depicted in **Figure** 5a, tap water, 5% NaCl solution, and alcohol were used as evaporation sources (RH: 25%, temperature: 20 °C). Experimentally, the different liquids exerted almost zero impact on the peak output performance of WE-TENG (transferred charges: ≈160 nC) and a significant impact on the operating period of the device. Compared to tap water and NaCl solution, alcohol reduced the operating period of the device to 17

s, owing to its high volatility and heat of vaporization. Figure 5b presents the output performance of WE-TENG at different load resistances (RH: 25%, temperature: 25 °C). The maximum peak power of WE-TENG was 0.42 mW, achieved at a load resistance of 900 MΩ. Figure 5c depicts the charging curve of WE-TENG for a single cycle at different load capacitances. A 200 nF capacitor could be charged to 9.8 V using the proposed WE-TENG for one cycle. Moreover, the WE-TENG exhibited excellent robustness, and the surface of the FEP film maintained a sound physical topography even after one week of usage (Figure S12, Supporting Information), owing to the use of flexible dielectric brushes. This feature further enhanced the long-time maintenance-free capability of WE-TENG as a power source in IoT terminals.

Environmental humidity is closely related to human productivity and life, and therefore, its detection is essential. Figure 5d illustrates the potential capabilities of the proposed WE-TENG in monitoring RH. Although all environmental factors, such as temperature, RH, and wind speed, affect the operating period, only RH affects the transferred charges of the device, and a high correlation exists between the latter two. Using Equation (3), it may be deduced that:

$$H = \frac{233.06 - Q_{\mathrm{H}}}{2.91} \tag{6}$$

Using electrical measuring equipment and computers, the transferred charges of WE-TENG could provide timely feedback regarding the RH in the environment. In addition to environmental monitoring, the device exhibited excellent power supply performance. As depicted in Figure 5e, WE-TENG could charge a 10 μF capacitor from 0 to 4.6 V within 200 s in an environment with a relative humidity of 25%, a temperature of 25 °C, and a wind speed of 0.5 m s^{-1}. The capacitor could power an electronic watch for 9 s after switching it on (Movie S2, Supporting Information). With sufficient water supply (lakes and seas or rainwater stored in rainwater harvesting systems) and connected to an automatic water dispenser (Note S3, Supporting Information), the drinking bird could receive inexhaustible water for the proposed WE-TENG to convert environmental heat into electricity, as illustrated in Figure 5f. This strategy would provide constructive guidance for the practical application of WE-TENG. Figure 5g illustrates the real-world application of the proposed WE-TENG, where the output signal could directly light two commercial LEDs of 2 W power each after full-wave rectification (Movie S3, Supporting Information). Therefore, the proposed WE-TENG could be directly applied to lake landscape design.

Metal corrosion in water has been one of the main issues troubling human life and productivity. Metal corrosion causes substantial economic losses and a severe threat to human lives. The traditional external circuit cathodic protection method requires an external power supply, which consumes additional energy, while remote transportation and electricity maintenance also become challenging. WE-TENG could effectively resolve this issue by utilizing water evaporation to generate power according to the local conditions. Figure 5h depicts a schematic diagram of the protection of carbon steel materials in the laboratory environment powered by WE-TENG. Experimentally, a full-wave rectifier bridge was used for converting the alternating current (AC) output of the WE-TENG to direct current (DC) energy and then injecting the energy into a capacitor (2.2 μF) to obtain a stable voltage output. Using NaCl solution with a mass fraction of 3.5% to simulate seawater, a rectangular carbon steel sheet with an area of 1.0 cm × 1.8 cm was connected to the cathode. A carbon electrode of the same area was connected to the anode. Another piece of the same size of carbon steel was immersed directly in salt water without cathodic protection and used as the control group. Figure 5i illustrates the surface appearance of carbon steel sheets after soaking for different periods with and without circuit protection. The proposed WE-TENG could provide electrical energy for self-powered corrosion prevention systems to protect carbon steel materials at the cathode. This strategy demonstrates the great potential of WE-TENG to provide electrical power in the waters.

3. Conclusion

In the present study, the drinking bird and TENG structures were combined to design WE-TENG, which relies on the evaporation process to spontaneously and sustainably convert heat energy in the environment into electrical energy. The proposed device effectively harnesses the energy involved in the atmospheric water cycle and expands the energy source of TENG. After rational structural optimization and material selection, the device exhibited an excellent electricity generation of 59.7 mJ mL^{-1}, which is three orders of magnitude higher than the previous droplet-based TENG when the same amount of tap water is consumed. The relationship between its output characteristics and the environmental parameters also provides the device with the potential for environmental monitoring. Furthermore, the device can operate uninterruptedly in water for an extended period and its flexible dielectric brushes and non-contact electrostatic induction positively influenced its lifetime. Therefore, our proposed WE-TENG allows for the utilization of tap water or other liquids, similar to oil, as fuel for the heat engine in electricity generation, significantly broadening the scope of available energy resources. Compared to wind, solar, and other green energy sources, evaporation is less limited by location sites, further expanding the application prospect of evaporation-generation technology. The present study would provide insight into the novel application directions for TENG and contribute to developing novel energy sources and mitigating the greenhouse effect.

4. Experimental Section

Preparation of the WE-TENG: The cylinder, disc, and rotor shaft models were constructed using modeling software. The light-curing molding technology was adopted to 3D print the above resin components. One of the curved surfaces of the cylinder (Figure S5a, Supporting Information; inner diameter: 19 cm; outer diameter: 20 cm; height: 6 cm) was extended outward into a 6 cm × 13.5 cm plane. The disc (Figure S5b, Supporting Information) had an outer diameter of 19 cm and a thickness of 5 mm, and its center was hollow with a diameter of 12.7 mm. The disc contained three sets of radial sectors with a central angle of 60°. The distal end of the radial sector was 90 mm from the center of the circle, while the proximal end was 10 mm from the same point. The length of the rotor shaft (Figure S5c, Supporting Information) was 6 cm, and the middle of the rotor shaft was equipped with a groove and a beak-shaped notch at the front. The shape of the rotor (Figure S5d, Supporting Information) was drawn using drawing software and then engraved using a computer numerical control machine. The thickness of the rotor was 2 mm, the circular angle of the

fan blade was 30°, and the length of the fan blade was 9 cm. The interval of the adjacent fan blades was 90°. In each fan blade, only the material of the outline and the central axis was retained, while the remaining material was eliminated. Drawing software was used for the drawing of the PCB, following which the electrodes were fabricated using the printed circuit board production process (Figures S5e and S4f, Supporting Information). The outer diameter of the circular PCB was 20 cm, and the PCB board was cut according to the radial area of the disc. The radial electrode is placed in the uncut area with a 30° center angle of the electrode, and a 12.7 mm diameter hole was added at the center of the circle of the inner PCB to ensure that the bearing could pass through the PCB compared to the outer PCB.

Fabrication of the WE-TENG: As depicted in Figure 2a(iii), first, the height of the rotor shaft on the glass tube of the drinking bird was confirmed, following which both structures were fixed together using the super glue; the silica gel solution was dripped onto the gap between the two structures to seal the gap. Using a spray bottle, the ultrasonically dispersed graphene solution was sprayed onto the surface of nylon fibers. The drinking bird structure was fixed inside the cylinder via the nested structure of the rotor shaft and the bearing. Next, the PCB (inside)–rotor–PCB (outside) structure was fixed successively on the outside of the disc. Four 5 mm spacers were placed at the edge between the two PCBs to ensure that the gap between them was 5 mm. A rotor formed of the FEP film was attached to a PC support and then connected to the rotor shaft, and the distance between the rotor and the PCBs was 1.5 mm. Finally, the NBR brush (length: 8 cm) was fixed in the radial direction outside the PCB to replenish the triboelectric charge for the FEP. The water trough (length: 4.8 cm; width: 3.5 cm; height: 3.5 cm) was fixed in front of the drinking bird to provide an evaporation source for the device.

Electrical Measurements of the WE-TENG: In order to prevent the interference of wind speed during the operation of the device, the evaluation related to the wind speed of 0 m s^{-1} was conducted inside a glove box (TONGRUN, AGB-4T, 50 cm × 50 cm × 90 cm). The temperature and humidity control system (DST, RA-51R) controlled the ambient temperature and RH. The different wind speeds were controlled using the gears of the electric fan and the distance from the electric fan to the device. The wind speed was measured using an anemometer (Aicevoos, AS-H6). A temperature and humidity meter (Anymetre, JB913A) was employed to measure the temperature and RH in the environment. A thermal imaging system was employed to capture the thermal images (Hikvision, DS-2TPH10–3AUF) in front of the main entrance of the School of Physical Science and Technology, Guangxi University, during the autumn season when the outdoor temperature was 28 °C. The electrostatic meter (Keithley, 6517) measured the device's open-circuit voltage, short-circuit current, transferred charge, and load current. The nanogenerator array test system (National Instruments, PXIe-1084) was used for measuring the synchronization signals on both sides of the rotor. The surface abrasion of the dielectric film was observed using a scanning electron microscope (Zeiss, Sigma 500).

Potential Field Simulation: Physical field simulation software was employed to simulate the two-dimensional potential distribution in space. FEP served as the dielectric film, and the induced electrodes were constituted of copper. The vertical distance between the dielectric film and the induction electrode was 1.5 mm, and the horizontal distance between the induction electrode and the dielectric film was 30 mm. The corresponding surface charge density was set according to the output performance of the device.

Supporting Information

Supporting Information is available from the Wiley Online Library or from the author.

Acknowledgements

The research was supported by the National Key R & D Project from the Ministry of Science and Technology (2021YFA1201603), the Natural Science Foundation of Guangxi Province (Grant No. 2021GXNSFAA075009), and the Specific Research Project of Guangxi for Research Bases and Talents (Grant No. GUIKEAD22035178).

Conflict of Interest

The authors declare no conflict of interest.

Data availability Statement

The data that support the findings of this study are available from the corresponding author upon reasonable request.

Keywords

Energy harvesting, heat energy, natural evaporation, triboelectric nanogenerators

Received: August 28, 2023
Revised: November 8, 2023
Published online: December 14, 2023

[1] K. Vohra, A. Vodonos, J. Schwartz, E. A. Marais, M. P. Sulprizio, L. J. Mickley, *Environ. Res.* **2021**, *195*, 110754.
[2] A. M. Levenda, I. Behrsin, F. Disano, *Energy Res. Soc. Sci.* **2021**, *71*, 101837.
[3] T. Oki, D. Entekhabi, T. I. Harrold, in *23rd General Assembly of the International-Union-of-Geodesy-and Geophysics*, IAG, Sapporo, Japan, **2003**, p. 225.
[4] H. Yao, M. Hashino, H. Yoshida, *J. Hydrol.* **1996**, *174*, 221.
[5] N. Kumar, J. H. Arakeri, in *IUTAM Symp. on Multiphase Flows with Phase Change Challenges and Opportunities*, IIT, Hyderabad, INDIA, **2014**, pp 108–115.
[6] J. Wei, B.-H. Fan, Y.i Pan, N.-N. Xing, S.-Q. Men, J. Tong, W. Guan, *J. Chem. Thermodyn.* **2016**, *101*, 278.
[7] L. Zhu, T. Ding, M. Gao, C. K. N. Peh, G. W. Ho, *Adv. Energy Mater.* **2019**, *9*, 1900250.
[8] L. Zhu, M. Gao, C. K. N. Peh, X. Wang, G. W. Ho, *Adv. Energy Mater.* **2018**, *8*, 1702149.
[9] G. Tan, S. Hao, R. C. Hanus, X. Zhang, S. Anand, T. P. Bailey, A. J. E. Rettie, X. Su, C. Uher, V. P. Dravid, G. J. Snyder, C. Wolverton, M. G. Kanatzidis, *ACS Energy Lett.* **2018**, *3*, 705.
[10] K. Liu, Y. L. Wu, C. Li, Y. Sun, Q. C. Li, C. Yang, X. H. Jia, M. R. Islam, Z. J. Wang, S. C. Qu, Z. G. Wang, *Adv. Mater. Technol.* **2021**, *6*, 8.
[11] B. N. J. Persson, U. Tartaglino, E. Tosatti, H. Ueba, *Phys. Rev. B* **2004**, *69*, 235410.
[12] T. Ding, K. Liu, J. Li, G. Xue, Q. Chen, L. Huang, B. Hu, J. Zhou, *Adv. Funct. Mater.* **2017**, *27*, 1700551.
[13] J. Sun, P. Li, J. Qu, X. Lu, Y. Xie, F. Gao, Y. Li, M. Gang, Q. Feng, H. Liang, X. Xia, C. Li, S. Xu, J. Bian, *Nano Energy* **2019**, *57*, 269.
[14] Y. Qin, Y. Wang, X. Sun, Y. Li, H. Xu, Y. Tan, Y.a Li, T. Song, B. Sun, *Angew. Chem., Int. Ed.* **2020**, *59*, 10619.
[15] F.-R.u Fan, Z.-Q. Tian, Z. Lin Wang, *Nano Energy* **2012**, *1*, 328.
[16] S. Nie, H. Guo, Y. Lu, J. Zhuo, J. Mo, Z. L. Wang, *Adv. Mater. Technol.* **2020**, *5*, 9.
[17] W. T. Li, L. Y. Wan, Y. Lin, G. L. Liu, H. Qu, H. G. Wen, J. J. Ding, H. Ning, H. L. Yao, *Nano Energy* **2022**, *95*, 9.
[18] J. J. Luo, Z. M. Wang, L. Xu, A. C. Wang, K. Han, T. Jiang, Q. S. Lai, Y. Bai, W. Tang, F. R. Fan, Z. L. Wang, *Nat. Commun.* **2019**, *10*, 9.
[19] H. M. Chen, Y. Xu, L. Bai, Y. Jiang, J. S. Zhang, C. Zhao, T. Li, H. L. Yu, G. F. Song, N. Zhang, Q. Q. Gan, *Adv. Mater. Technol.* **2017**, *2*, 7.

[20] Y. Xie, S. Wang, S. Niu, L. Lin, Q. Jing, J. Yang, Z. Wu, Z. L. Wang, *Adv. Mater.* **2014**, *26*, 6599.
[21] Y. J. Zou, J. Xu, K. Chen, J. Chen, *Adv. Mater. Technol.* **2021**, *6*, 16.
[22] Z. Y. Huo, Y. J. Kim, I. Y. Suh, D. M. Lee, J. H. Lee, Y. Du, S. Wang, H. J. Yoon, S. W. Kim, *Nat. Commun.* **2021**, *12*, 11.
[23] Y. Bian, T. Jiang, T. Xiao, W. Gong, X. Cao, Z. Wang, Z. L. Wang, *Adv. Mater. Technol.* **2018**, *3*, 7.
[24] C. Yan, Y. Y. Gao, S. L. Zhao, S. L. Zhang, Y. H. Zhou, W. L. Deng, Z. W. Li, G. Jiang, L. Jin, G. Tian, T. Yang, X. Chu, D. Xiong, Z. X. Wang, Y. Z. Li, W. Q. Yang, J. Chen, *Nano Energy* **2020**, *67*, 5.
[25] L.i Dong, M. Wang, J. Wu, C. Zhu, J. Shi, H. Morikawa, *Adv. Fiber Mater.* **2022**, *4*, 1486.
[26] H. G. Wen, P. Y. Yang, G. L. Liu, S. X. Xu, H. L. Yao, W. T. Li, H. Qu, J. J. Ding, J. Y. Li, L. Y. Wan, *Nano Energy* **2022**, *93*, 9.
[27] Q. X. Zhang, M. He, X. X. Pan, D. D. Huang, H. H. Long, M. S. Jia, Z. Q. Zhao, C. Zhang, M. Y. Xu, S. S. Li, *Nano Energy* **2022**, *103*, 10.
[28] Q. Zheng, B. Shi, F. Fan, X. Wang, L. Yan, W. Yuan, S. Wang, H. Liu, Z. Li, Z. L. Wang, *Adv. Mater.* **2014**, *26*, 5851.
[29] S. Sardana, H. Kaur, B. Arora, D. K. Aswal, A. Mahajan, *ACS Sens.* **2022**, *3*, 312.
[30] P. Bai, G. Zhu, Z.-H. Lin, Q. Jing, J. Chen, G. Zhang, J. Ma, Z. L. Wang, *ACS Nano* **2013**, *7*, 3713.
[31] H. Y. Li, L.i Su, S. Y. Kuang, C. F. Pan, G. Zhu, Z. L. Wang, *Adv. Funct. Mater.* **2015**, *25*, 5691.
[32] L. Lin, S. Wang, S. Niu, C. Liu, Y. Xie, Z. L. Wang, *ACS Appl. Mater. Interfaces* **2014**, *6*, 3031.
[33] Y. Chen, B. Xie, J. Long, Y. Kuang, X. Chen, M. Hou, J. Gao, S. Zhou, B.i Fan, Y. He, Y.-T. Zhang, C.-P. Wong, Z. Wang, N.i Zhao, *Adv. Mater.* **2021**, *33*, 2104290.
[34] W. Xu, H. Zheng, Y. Liu, X. Zhou, C. Zhang, Y. Song, X.u Deng, M. Leung, Z. Yang, R. X. Xu, Z. L. Wang, X. C. Zeng, Z. Wang, *Nature* **2020**, *578*, 392.
[35] L. Wang, Y. Song, W. Xu, W. Li, Y. Jin, S. Gao, S. Yang, C. Wu, S. Wang, Z. Wang, *EcoMat* **2021**, *3*, e12116.
[36] J. Dong, C. Xu, L. Zhu, X. Zhao, H. Zhou, H. Liu, G. Xu, G. Wang, G. Zhou, Q. Zeng, Q. Song, *Nano Energy* **2021**, *90*, 106567.
[37] X. Xu, Y. Wang, P. Li, W. Xu, L. Wei, Z. Wang, Z. Yang, *Nano Energy* **2021**, *90*, 106573.
[38] N. Zhang, H. Gu, K. Lu, S. Ye, W. Xu, H. Zheng, Y. Song, C. Liu, J. Jiao, Z. Wang, X. Zhou, *Nano Energy* **2021**, *82*, 105735.
[39] Y. Li, M. Wang, C. Zhang, C.-C. Wang, W. Xu, S. Gao, Y. Zhou, C.-T.a Wang, Z. Wang, *Adv. Opt. Mater.* **2022**, *10*, 2102274.
[40] L. Wang, W. Li, Y. Song, W. Xu, Y. Jin, C. Zhang, Z. Wang, *Adv. Funct. Mater.* **2022**, *32*, 2206705.
[41] N. Zhang, H. Zhang, Z. Liu, W. Xu, H. Zheng, Y. Song, Z. Wang, X. Zhou, *Nano Energy* **2023**, *106*, 108111.
[42] C. X. Lu, C. B. Han, G. Q. Gu, J. Chen, Z. W. Yang, T. Jiang, C. He, Z. L. Wang, *Adv. Eng. Mater.* **2017**, *19*, 8.
[43] B. L. Cheng, Q. Xu, Y. Q. Ding, S. Bai, X. F. Jia, Y. D. C. Yu, J. Wen, Y. Qin, *Nat. Commun.* **2021**, *12*, 8.
[44] K. Wang, Z. R. Qiu, J. X. Wang, Y. Liu, R. Chen, H. An, J. H. Park, C. H. Suk, C. X. Wu, J. T. Lin, T. W. Kim, *Nano Energy* **2022**, *93*, 10.